

RESEARCH ARTICLE

10.1002/2017JE005261

Special Section:

Investigations of the Bagnold Dune Field, Gale crater

Key Points:

- Bagnold Dunes Campaign corresponds to the first in situ characterization of active dune field
- Bagnold dunes lack <100 μm and > 1 mm grains
- Bagnold dunes are overall similar to Aeolis Palus soils in composition but are depleted in volatile-rich amorphous component and present slightly more olivine

Correspondence to:

A. Cousin,
agnes.cousin@irap.omp.eu

Citation:

Cousin, A., et al. (2017), Geochemistry of the Bagnold dune field as observed by ChemCam and comparison with other aeolian deposits at Gale Crater, *J. Geophys. Res. Planets*, 122, 2144–2162, doi:10.1002/2017JE005261.

Received 9 JAN 2017

Accepted 20 JUN 2017

Accepted article online 27 JUN 2017

Published online 23 OCT 2017

Geochemistry of the Bagnold dune field as observed by ChemCam and comparison with other aeolian deposits at Gale Crater

Agnes Cousin¹, Erwin Dehouck¹ , Pierre-Yves Meslin¹ , Olivier Forni¹ , Amy J. Williams² , Nathan Stein^{3,4} , Olivier Gasnault¹ , Nathan Bridges⁵ , Bethany Ehlmann^{4,6} , Susanne Schröder⁷ , Valérie Payré⁸ , William Rapin¹, Patrick Pinet¹, Violaine Sautter⁹ , Nina Lanza¹⁰ , Jérémie Lasue¹ , Sylvestre Maurice¹, and Roger C. Wiens¹⁰ 

¹Institut de Recherche en Astrophysique et Planétologie, Université de Toulouse, CNRS, UPS, CNES, Toulouse, France,²Department of Physics, Astronomy, and Geosciences, Towson University, Towson, Maryland, USA, ³Division of Geological and Planetary Sciences, Caltech University, Pasadena, California, USA, ⁴Division of Geological and Planetary Sciences, California Institute of Technology, Pasadena, California, USA, ⁵Applied Physics Laboratory, Laurel, Maryland, USA, ⁶Jet Propulsion Laboratory, California Institute of Technology, Pasadena, California, USA, ⁷DLR, Berlin, Germany,⁸GeoRessources, Nancy, France, ⁹Museum National d'Histoire Naturelle, Paris, France, ¹⁰LANL, Los Alamos, New Mexico, USA

Abstract The *Curiosity* rover conducted the first field investigation of an active extraterrestrial dune. This study of the Bagnold dunes focuses on the ChemCam chemical results and also presents findings on the grain size distributions based on the ChemCam Remote Micro-Imager and Mars Hand Lens Imager images. These active dunes are composed of grains that are mostly <250 μm . Their composition is overall similar to that of the aeolian deposits analyzed all along the traverse (“Aeolis Palus soils”). Nevertheless, the dunes contain less volatiles (Cl, H, and S) than the Aeolis Palus soils, which appear to be due to a lower content of volatile-rich fine-grained particles (<100 μm) or a lower content of volatile-rich amorphous component, possibly as a result of (1) a lower level of chemical alteration, (2) the removal of an alteration rind at the surface of the grains during transport, (3) a lower degree of interaction with volcanic gases/aerosols, or (4) physical sorting that removed the smallest and most altered grains. Analyses of the >150 μm grain-size dump piles have shown that coarser grains (150–250 μm) are enriched in the mafic elements Fe and Mn, suggesting a larger content in olivine compared to smaller grains (<150 μm) of the Bagnold dunes. Moreover, the chemistry of soils analyzed in the vicinity of the dunes indicates that they are similar to the dune material. All these observations suggest that the olivine content determined by X-ray diffraction of the <150 μm grain-size sample should be considered as a lower limit for the Bagnold dunes.

Plain Language Summary The *Curiosity* rover, which is exploring the Gale Crater on Mars, has been investigating a dune field. This is the first time an active and extensive dune field is explored by a rover on Mars, and therefore, *Curiosity* used all the instruments on board in order to better understand how the dunes can form and with what processes and also to assess their chemistry. This in situ investigation was a great opportunity to compare with orbital data. Our work is focusing on chemical data from the ChemCam instrument, as well as on grain size distributions from the image analyses of two cameras. We show that, overall, the dunes are similar in chemistry to the soils analyzed along the traverse, but they are depleted in H, Cl, and S, suggesting that they contain less fine-grained particles or less amorphous component (which is known to be enriched in such elements). This could be due to several processes that we try to investigate. Also, we show that the coarser grains of the dunes (150–250 μm) are enriched in Fe and Mn, probably due to an enrichment in olivine.

1. Introduction and Context

1.1. MSL Overview (Payload and Traverse)

The Mars Science Laboratory (MSL) rover *Curiosity* landed in August 2012 in Gale Crater, located at the northern edge of the Noachian highlands on Mars. This crater is 154 km in diameter [Anderson and Bell, 2010] and contains a central mound informally called “Mount Sharp” (official IAU name: Aeolis Mons) that is known to have exposed phyllosilicates and sulfates based on orbital observations [Milliken et al., 2010]. As of November 2016, *Curiosity* has driven ~15 km. The journey started at the Bradbury landing site, in the

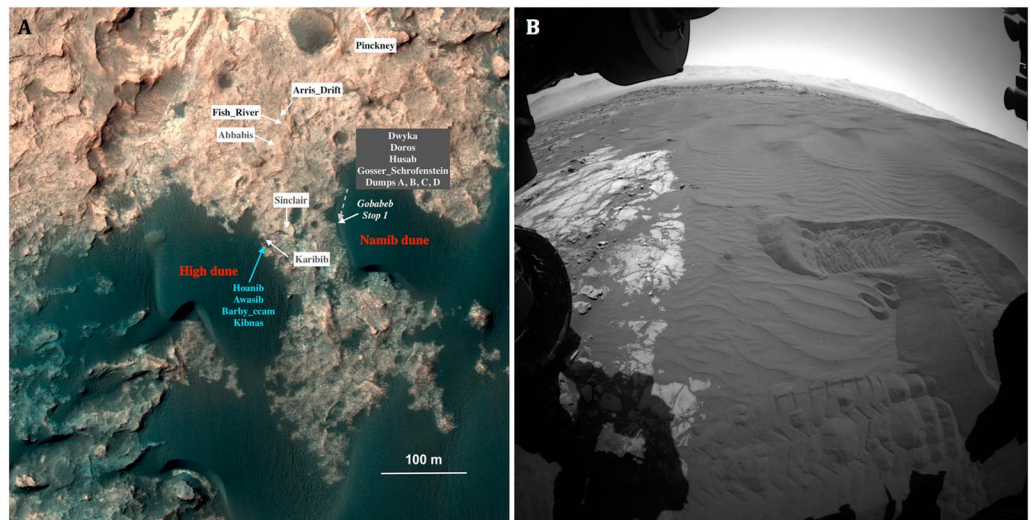


Figure 1. (A) Localization of High and Namib dunes (in red) in the Bagnold dune field. ChemCam targets investigated in High dune are indicated in blue. The Gobabeb stop is located as well as the ChemCam targets sampled at this place (in grey). Soil targets in the vicinity of the dunes are indicated in black. (B) View of the Gobabeb stop from Curiosity's front hazardous avoidance camera (image credit: NASA/JPL-Caltech).

hummocky plains of Aeolis Palus, located north/northwest of Mount Sharp. The rover crossed these hummocky plains during the first 60 sols (Martian days) and then entered a region named Yellowknife Bay, where exposed sedimentary rocks, namely, mudstones and sandstones, were interpreted as fluvio-lacustrine deposits [Grotzinger *et al.*, 2014; McLennan *et al.*, 2014]. After leaving Yellowknife Bay, the rover started a long traverse across Aeolis Palus to the other main mission objective, the basal layers of Mount Sharp, which were reached at Pahrump Hills, on sol 750 [Grotzinger *et al.*, 2015].

In order to access higher layers of Mount Sharp, *Curiosity* had to cross a large active dune field informally called "Bagnold dunes." As seen from orbit, these dunes show both barchans and longitudinal morphologies and appear enriched in mafic components [Rogers and Bandfield, 2009; Milliken *et al.*, 2010]. Moreover, Seelos *et al.* [2014] have shown the existence of active grain sorting processes in the dunes, as the barchans appear enriched in olivine compared to the longitudinal dunes that are more pyroxene-rich. Lapotre *et al.* [2017] have found evidence for composition and grain size sorting within the dune field and have hypothesized that multiple sand sources (with different travel distances) may be mixed in the Bagnold dunes.

The Mars Exploration Rovers *Spirit* and *Opportunity* investigated small ripple and dune fields at Gusev and Meridiani [Sullivan *et al.*, 2008; Chojnacki *et al.*, 2015], but the crossing of the Bagnold dunes by *Curiosity* provided the very first opportunity for in situ characterization of an extensive, active dune field on another planet. Thus, a dedicated campaign (between sols 1181 and 1254) was conducted in order to investigate these dunes. The main objective of this campaign was to acquire chemical, geomorphological, and textural data on these active dunes in order to increase the understanding of past and current aeolian processes on Mars [Bridges and Ehlmann, 2017].

This campaign was organized in several main steps starting with an approach from the north (Figure 1). The first step was to perform a mobility test [Arvidson and Maimone, 2016], which was executed on a sandy patch associated with High dune, and to acquire opportunistic science measurements. The second step was the detailed investigation of Namib dune. The rover first stopped in front of the main Namib dune slip face to perform remote-sensing observations, then moved to a secondary slip face in order to perform in situ investigations at a site referred to as "Gobabeb." The overall Bagnold dune campaign is described in more detail in Bridges and Ehlmann [2017], and geomorphological observations are presented in Bridges *et al.* [2017].

The entire *Curiosity* payload was used during this campaign. The Dynamic Albedo of Neutrons (DAN) instrument performed neutron spectroscopy along the traverse to obtain H and Cl content of ground beneath the rover [Mitrofanov *et al.*, 2012]. At Namib dune, before leaving the workspace, the rover was reoriented in order to get the best estimate of neutron flux from the dune material. The imagers, including MastCam

Table 1. List of Targets Analyzed by ChemCam in the Bagnold Dune Field and in Their Vicinity

Aeolian Deposits in the Vicinity of the Dunes		
Target Name and Type	Sequence ID	Sol Number
Pinckney—aeolian	ccam02155	sol 1155
Arris_Drift—aeolian	ccam01162	sol 1162
Fish_River	ccam02167	sol 1167
Abbabis	ccam01169	sol 1169
Sinclair—aeolian	ccam01174	sol 1174
Karibib—aeolian	ccam01177	sol 1177
<i>High Dune Data</i>		
Hoanib disturbed	ccam01182	sol 1182
Awasib disturbed	ccam02182	sol 1182
Barby_ccam undisturbed	ccam01184	sol 1184
Kibnas undisturbed	ccam02184	sol 1184
<i>Namib Dune Data</i>		
Dwyka undisturbed	ccam07232	sol 1232
Doros—wall scuff	ccam02225	sol 1225
Husab—floor scuff	ccam04235	sol 1235
Gosser_Schrofenstein wall disturbed	ccam02239	sol 1239
Dump A	ccam03228	sol 1228
Dump B	ccam04228	sol 1228
Dump C	ccam06232	sol 1232
Dump D	ccam06232	sol 1232

[Malin *et al.*, 2010; Bell *et al.*, 2012], Mars Hand Lens Imager (MAHLI) [Edgett and Yingst, 2013], and the ChemCam Remote Micro-Imager (RMI) [Maurice *et al.*, 2012] were used to look for sand movement between several sols, as well as to better constrain the geomorphology of the dune field, and to obtain statistics on grain sizes and colors. The MastCam multispectral analysis capabilities and ChemCam passive visible/near-infrared spectroscopy capabilities were also used [Johnson *et al.*, 2017]. In situ investigations at Namib dune consisted of trenching and scooping some of the dune material, with different size fractions separated by sieving <150 μm , >150 μm , 150 μm to 1 mm, and >1 mm fractions. The <150 μm and 150 μm to 1 mm size fractions were then delivered to Sample Analysis at

Mars (SAM) for measurement of volatile elements, and the smallest size fraction (<150 μm) was also delivered to CheMin for mineralogy quantification. Chemical data were acquired by both the Alpha-Particle X-ray Spectrometer (APXS) and ChemCam instruments on different parts of the Namib dune: on the crest, in a trough, in a trench (scuff), and on piles of processed samples that were dumped to the ground after being sieved. See Mahaffy *et al.* [2012] for a detailed description of the SAM instrument, Blake *et al.* [2012] for CheMin, Campbell *et al.* [2012] for APXS, and Wiens *et al.* [2012] and Maurice *et al.* [2012] for ChemCam.

This study focuses on data from the ChemCam instrument, which uses the laser-induced breakdown spectroscopy (LIBS) technique (see next section) to determine the chemical composition of the targets. Owing to its remote sensing ability (up to 7 m from the rover), ChemCam has been intensively used during the mission; as of November 2016, it has performed 116 observation points on soil targets. It is therefore interesting to compare the composition of the active Bagnold dunes with those of the soils encountered along the traverse. These analyses can better constrain soil chemistry, delineate any possible relationship between the soils and active dunes, and elucidate both formation pathways to address whether the soils and active dunes are made of the same type of material and whether they have experienced the same level and type of chemical alteration.

1.2. Data Set Used for This Study

Within the Bagnold dune field, ChemCam sampled 12 targets (Figure 1 and Table 1). At High dune, two trench targets (Awasib and Hoanib) were analyzed, as well as two undisturbed ones: Barby_ccam3 near a crest and Kibnas in a nearby trough. This was on sols 1182 and 1184. At Namib dune, ChemCam analyzed three scuffed targets (Doros, Husab, and Gosser_Schofenstein), one undisturbed target (Dwyka), and four dump piles, i.e., small piles of sand made by the Sample Acquisition/Sample Processing and Handling subsystem of the rover [Anderson *et al.*, 2012]: dump A (<150 μm), dump B (>150 μm), dump C (150 μm –1 mm), and dump D (>1 mm). All the samples analyzed by ChemCam are reported in Table 1, with the corresponding observation sol and parameters.

In the present study, data obtained in the northern vicinity of the Bagnold dune field are also taken into account. They correspond to six dark and sandy patches encountered between sols 1155 and 1177, just before arriving at High dune. These targets are hereafter referred to as “nearby soils.”

Data from the Bagnold dunes and nearby soils are compared here with all the previous fine-grained soils previously analyzed by ChemCam along the traverse [Meslin *et al.*, 2013; Cousin *et al.*, 2014b], including the soils analyzed using the “blind target mode” [Cousin *et al.*, 2014a]. This automatic mode consisted of pointing ChemCam to -42° on the right side of the rover after a drive. This procedure allowed for a good LIBS performance (constant distance to target ~ 3 m) and an unbiased sampling of soils. These fine-grained soils encountered up to Pahrump Hills are hereafter referred to as “Aeolis Palus soils.” This is a data set of 34 targets corresponding to 116 observation points.

2. Methods

2.1. ChemCam Instrument: Small-Scale Analysis

The ChemCam instrument uses the laser-induced breakdown spectroscopy (LIBS) technique, which consists of focusing a pulsed laser on a target in order to ablate it. The ablated material forms a high-temperature plasma, which contains all the elemental species present in the sampled target. When excited ions and atoms from the plasma relax to their ground state, they emit photons at a characteristic wavelength typical of the element. Analysis of this plasma by optical spectroscopy with proper calibration leads to the chemical composition of the target. ChemCam has three spectrometers, from the ultraviolet to the near infrared (240–900 nm). This technique, which is new in planetary exploration, enables analyses of targets that are up to 7 m from the instrument and without any preparation. This ability leads to more data acquisition than contact instruments and a larger variety of rock and soil targets.

One unique feature of the LIBS technique is the small spatial scale of its analyses, with a diameter between 350 and 550 μm depending on distance [Maurice *et al.*, 2013]. This enables the sampling of pure phases when minerals are large enough ($>$ LIBS spot size). Multiple observation points are commonly performed on each target (from 5 to 16 points) in order to determine the bulk composition. Each observation point consists of at least 30 shots, which gives the possibility to investigate potential chemical variation with depth (typically a few millimeters in soils). Averaging these 30 shots, on the other hand, provides a better signal-to-noise ratio for elements with lower sensitivity, including some minor and trace elements [Wiens *et al.*, 2013].

2.2. Quantification of Major and Minor Elements

The LIBS technique is sensitive to most chemical elements. The quantification of major element oxides (SiO_2 , TiO_2 , Al_2O_3 , FeO_T , MgO , CaO , Na_2O , and K_2O) is performed using a combination of two multivariate techniques: the “partial least squares” (PLS) and the “independent component analysis” (ICA). An improved calibration was completed in 2015, expanding the standard database from 65 to 450 standards and enabling a better determination of major elements [Wiens *et al.*, 2015; Clegg *et al.*, 2017]. The PLS method uses different emission lines of a given element and compares them to known standards analyzed in a test bed on Earth [Clegg *et al.*, 2009; Wiens *et al.*, 2013]. This technique has been updated by using submodels depending on the range of compositions for each element [R. B. Anderson *et al.*, 2017]. The ICA technique used to classify ChemCam data [Forni *et al.*, 2009, 2013; Lasue *et al.*, 2011] is derived from blind source separation research [Hyvarinen, 2001] and identifies different statistically independent components, allowing spectra to be sorted from these components. Regression curves are obtained for each element, between the ICA score and the known compositions of the reference spectra.

The accuracy of ChemCam major-element compositions is estimated by calculating the root mean-square-error of prediction (RMSEP) for a representative test set of geostandards for each major element. This RMSEP varies as a function of abundance and is calculated by observing the errors of the test-set standards over the range of abundances. In this work, typical accuracies and precisions are reported in Table 2. This precision is determined from the standard deviation of multiple observations performed on the shergottite calibration target from sols 271 to 357 [Blaney *et al.*, 2014]. The shergottite calibration target [Fabre *et al.*, 2011] is a homogeneous glassy target onboard Curiosity that has a chemical composition similar to the shergottite meteorites [McSween, 1994]. The Yellowknife Bay mudstone, a fine-grained and homogeneous type of target, provides an upper limit for this precision, allowing for some slight variation in the mudstone compositions [Mangold *et al.*, 2015]. These are generally consistent with precision from Blaney *et al.* [2014].

MnO is quantified using a univariate technique comparing the MnO content of a dedicated suite of samples with the LIBS signal of the Mn emission line [Lanza *et al.*, 2014]. Its accuracy is 2.2 wt % for $\text{MnO} < 10$ wt %

Table 2. Average Accuracy (in wt %) Obtained on All the Targets Used in This Study and Precision (in wt %) of the ChemCam Quantification^a

	SiO ₂	TiO ₂	Al ₂ O ₃	FeO	MgO	CaO	Na ₂ O	K ₂ O
Average accuracy of the study (wt %)	5.2	0.5	3.4	4.2	2.1	2.4	0.6	0.6
Average precision of ChemCam data (wt %)	1.5	0.14	0.57	1.8	0.49	0.42	0.49	0.14

^aThe accuracy represents the error on the quantification for each major element and is calculated from the root-mean-square error of prediction (RMSEP) computed from the geostandard database. The precision represents the reproducibility of the quantification, performed on the ChemCam calibration target shergottite, between sols 271 and 357 [from *Blaney et al., 2014*].

[*Lanza et al., 2014*]. Nevertheless, targets in this study contain much less MnO (<3 wt %), and therefore, the accuracy for MnO quantification should be better than 2.2 wt %. S and Cl are not yet quantified with ChemCam. They both suffer from matrix effects; the S main emission lines overlap with those of other elements within the ChemCam spectrometer ranges, and the Cl detection limit is low [*D. Anderson et al., 2017*]. Therefore, we mainly use qualitative observations for these elements, such as the peak area of the line of interest after normalization of the spectrum. Regarding hydrogen, its quantification in soils is still in progress [*Rapin et al., 2017*], and here we present the H signal from the ICA multivariate analysis [*Forni et al., 2013*].

2.3. Grain Size Determination From RMI

In addition to LIBS spectra, ChemCam also collects images using the Remote Micro-Imager (RMI). The RMI has a pixel angular size of 19.6 μ rad and produces 1024 \times 1024 pixel panchromatic images with a circular field of view of 20 mrad [*Le Mouélic et al., 2015*]. The RMI has a spatial angular resolution of \sim 2 pixels at best focus [*Langevin et al., 2013; Le Mouélic et al., 2015*], which will be rounded to \sim 50 μ rad for this work. For each analysis, at least 2 RMIs are taken: one before and one after the laser shots. When the observation spans a wide area, additional RMIs are inserted between the LIBS analyses to ensure that the images fully cover the sampled area. The RMI mosaics presented in this paper provide the textural context that is therefore relevant for interpreting the LIBS chemical data.

To aid in understanding the soils' variability, we conducted a survey of grain sizes using RMI mosaics. The RMI has a narrow depth of focus (\sim 1 cm at a 2 m distance) [*Maurice et al., 2012*] that limits grain resolution outside of the best focus field in the mosaics. Each target was evaluated by determining the range of grain diameters and grain size distribution of the resolvable grains.

To determine the scale of each image, we used the known pixel scale (θ) of the RMI (19.6 μ rad) and the distance to the target (d) to calculate the size of a pixel (x) at that distance: $x = d \tan \theta$. Distances recorded for each RMI in a mosaic are, in most cases, only slightly different from each other (average distance \sim 2.8 m, with only a few centimeters of differences between two images of a mosaic)—therefore, the size of a pixel in one mosaic is constant, as the d value does not vary significantly.

Grain size was measured by hand in each ChemCam target using the National Institute of Health software package ImageJ [*Schneider et al., 2012*], which is a program for image processing and analysis. Particle size analyses of RMI images were performed for each target using a photographic grid-by-number sampling approach [*Graham et al., 2005*]. This conventional method would set the grid spacing at twice the maximum grain diameter [*Graham et al., 2005*]. However, this aspect of the grid-by-number sampling approach is not feasible for RMI images with a narrow depth of focus because the range of grain sizes in a given RMI image could encompass 1–2 orders of magnitude. This greatly reduces the number of smaller diameter grains measured when the grid spacing is set at twice the maximum grain diameter [*Graham et al., 2005; Karunatillake et al., 2014a, 2014b*] and thereby defeats the purpose of the measuring campaign, which was to assess the average grain size in RMI images.

A grid with 15 mm² dimensions was overlaid on the RMI mosaics to allow an unbiased method to measure the variety of grains at every grid intersection without the need to measure every grain in the mosaic, which was not feasible. Additionally, maintaining a 15 mm² grid over each RMI target was key to keep measurements between different RMI images consistent and was appropriate, as RMI images in the Bagnold Dunes Campaign were taken at similar standoff distances (range 2.3 m to 3.6 m). Target images ranged from

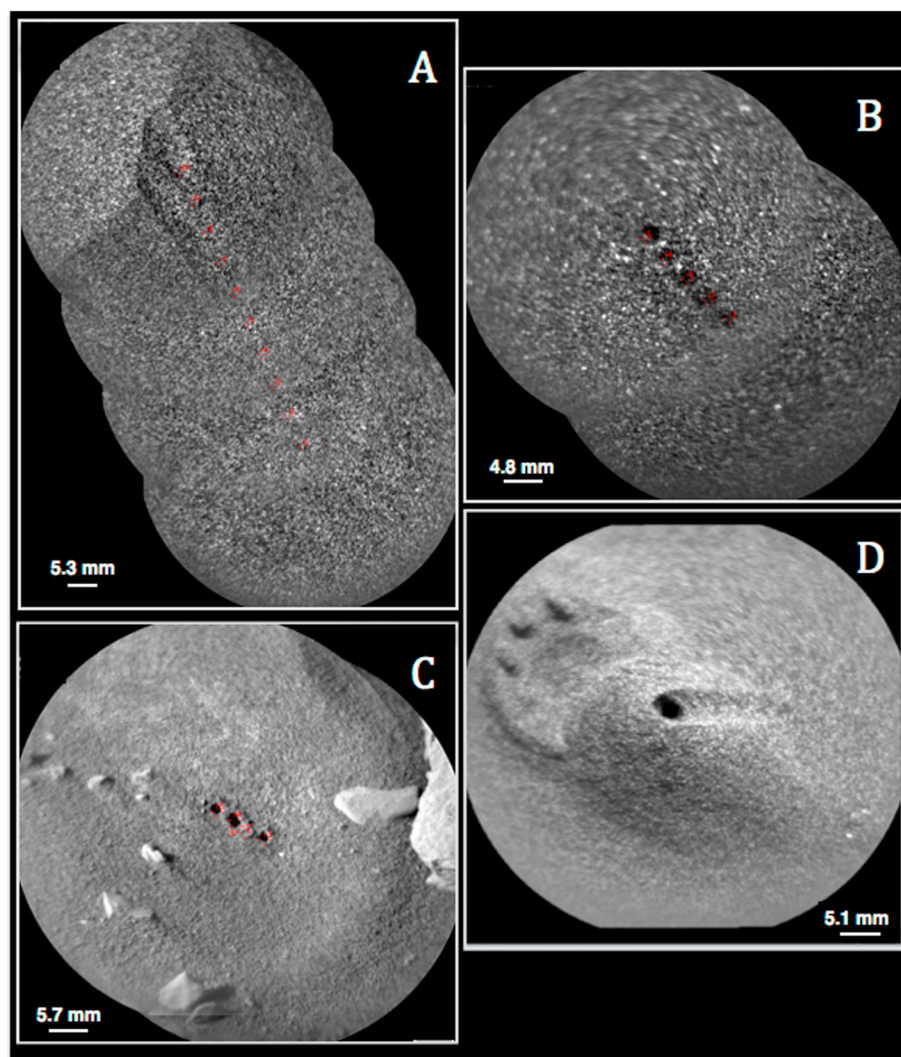


Figure 2. RMI images of some of the Bagnold dune targets sampled by ChemCam. (A) Doros (trench); (B) Barby_ccam3 (undisturbed); (C) Abbabis (soil located north of Bagnold dune field); (D) dump A corresponding to the $<150 \mu\text{m}$ sieve size. The red crosses in mosaics A, B, and C correspond to the exact location of each point analysis.

single frames to multiple mosaicked frames (see Figure 2), with mosaicked frames inherently containing a greater number of grains than single frame images. Because of the nonuniform nature of the RMI images (i.e., single versus mosaicked frames), the conventional node placement of a 20×20 grid [McGlynn *et al.*, 2011] was not appropriate. Maintaining the 15 mm^2 grid allowed for the most comparable data between RMI targets, and grids ranged from 29×17 to 14×14 nodes. The 15 mm^2 grid yielded on average 318 (range 196 to 493) individual points of measurement (i.e., nodes), comparable to other studies of extraterrestrial sediments [McGlynn *et al.*, 2011]. Lastly, although poorly and very poorly sorted sediments may not be fully characterized by the use of mean grain sizes, the approach is demonstrated to broadly distinguish between groups of sediments (i.e., dust, sand, and pebbles) [McGlynn *et al.*, 2012], and sample targets with more well sorted sediments, such as those in the Bagnold dunes, should be comparably or better characterized with mean grain sizes.

Grain size was determined by measuring the longest axis of the grain at the grid intersection point, which may be underestimated if the grain is oriented such that the long axis is not visible [Yingst *et al.*, 2013]. Without optimal grain reflectance contrast, grains that were smaller than 0.5 mm were difficult to consistently measure, even though this is 3 or 4 times more than the spatial resolution. Therefore, in this study, the lowest measurable grain size is set to 0.5 mm and grains smaller than 0.5 mm were all characterized as “fines.” Grain

sizes greater than this cutoff limit were binned according to the Wentworth scale [Wentworth, 1922] (pebble = 4–64 mm, granule = 2–4 mm, very coarse sand = 1–2 mm, coarse sand = 0.5–1 mm). The size of very small grains may be overestimated with 2-D grain size analyses due to erratic grain size frequencies in small grains, the blurring of grain edges due to pixelation, and the inability to measure grains that are smaller than the pixel size [Friday *et al.*, 2013]. To mediate this potential concern, the method of Yingst *et al.* [2008] was utilized, requiring all measurable grains to be composed of at least 5 pixels.

The grain size distribution was determined for each RMI mosaic acquired on Bagnold dune samples. From the total number of nodes, points that were not resolvable (i.e., out of focus, overlying pore space, or shadowed region) were subtracted from the total. Then the percentage of grains <0.5 mm (called “fines”) was calculated. The percentage of remaining grains larger than 0.5 mm was binned according to grain size, as described above. In this way, the percentage of each grain size class was quantified in each RMI mosaic.

2.4. Grain Size Determination From MAHLI for Dump Piles

Grain size distributions were measured for four sieved dump piles at Namib dune: “A” (<150 μm fraction), “B” (>150 μm fraction), “C” (<1 mm fraction), and “D” (>1 mm fraction). MAHLI images collected from a ~ 1 cm standoff distance provide a spatial resolution better than 19 μm per pixel for each dump pile, allowing smaller grains to be resolved. Particle size analyses of MAHLI images were performed for each pile by hand using a grid-by-number count. A regularly spaced grid with a spacing twice that of the largest grain diameter was superimposed on a MAHLI image of each discard pile, and the maximum and intermediate (the second longest of the three principal grain axes) diameter of the grain at the intersection of each grid point was recorded, yielding several hundred grain measurements per discard pile. The grid spacing was selected to minimize the number of intersections that fell on the same or adjacent grains while maximizing the number of grains counted. Portions of the images that were out of focus due to vertical relief were not included in the count. The images were histogram normalized to account for different lighting conditions; color and translucence were identified visually. Counts were performed over approximately the same area for each pile, and the grains were assumed to have settled such that the intermediate and maximum axes were orthogonal to the viewing geometry. Uncertainties in the measured particle size distributions stem from uncertainties in the MAHLI depth of field, which is used to estimate the pixel scale of each MAHLI image [Yingst *et al.*, 2016].

3. Results

3.1. Grain Size Distribution

For this study, images acquired on dump piles, disturbed and undisturbed dune material, and on nearby soils have been taken into account.

We measured grain sizes in RMI images of 12 named targets from the Bagnold dune area, including nearby soils (sols 1155–1234). The RMI images contain mainly loose grains reducing the likelihood of different grain sizes in the out-of-focus areas (Figure 2). Overall, the dunes and nearby soils are mostly composed of grains smaller than coarse sand (<0.5 mm), thus not measurable by our method. These grains, which represent more than 50% of the grains in all mosaics (Table 3), are hereafter referred to as “fines” following the terminology used in previous studies of soils with ChemCam [Meslin *et al.*, 2013; Cousin *et al.*, 2014b]. Considering only the measurable grains (>0.5 mm), they range in size from coarse sand to pebble; the largest grain was 25.1 mm (Table 2). The presence of several granules on the Abbabis target mosaic explains its much higher average grain size (3.8 mm) compared to other targets (0.5–0.7 mm), but these granules were not sampled with LIBS.

MAHLI images of the sieve dumps (Figure 3) have been analyzed using the methodology described in section 2.4. Each of the dump piles contains a mixture of opaque or translucent grains. Concerning the color of the grains, when the difference between black, brown, and dark green grains was too difficult to distinguish, we classified the grains as “dark” rather than giving a precise color. Grains of all colors and transparency are present in all four dumps, but only those with abundance $>1\%$ are discussed and included in Figure 4.

Dump A (from the <150 μm sieve) contains grains with an average intermediate and maximum axis diameter of 103 μm (± 1 μm) and 142 μm (± 2 μm), respectively, and the distribution ranges from ~ 50 to ~ 200 μm if the single-grain outliers are not considered (Figure 4a). Dark grains are most abundant (42%; Figure 4a).

Table 3. Summary of the Grain Size Results From the RMI Analyses^a

Target Name	Sol	Average Grain Diameter (mm)	Maximum Grain Diameter (mm)	Percent of Grains >0.5 mm in Diameter	Percent of Grains <0.5 mm in Diameter (Fines)	Number of Grains >0.5 mm Measured
Pinckney	1155	1.38	8.360	45.8%	54.2%	11
Arris_Drift	1162	0.70	1.167	20.0%	80.0%	6
Fish_River	1167	0.67	0.896	28.0%	72.0%	7
Abbabis	1169	3.76	25.116	52.8%	47.2%	19
Sinclair	1174	0.65	0.879	47.1%	52.9%	8
Karibib	1177	0.67	1.126	44.8%	55.2%	39
Awasib	1182	0.57	0.690	6.0%	94.0%	3
Hoanib	1182	0.58	0.578	8.0%	92.0%	1
Barby	1184	0.62	0.712	46.7%	53.3%	14
Kibnas	1184	0.64	0.872	19.7%	80.3%	12
Doros	1225	0.58	0.593	2.8%	97.2%	2
Dwyka	1232	nd	nd	0.0%	100.0%	0

^aThe average grain diameter takes into account only grains that are >0.5 mm (see section 2.3 for more details). When the target is only composed of material lower to 0.5 mm in size (which is the lowest measurable grain size with RMI), the assessment of the grain diameter has not been possible, and therefore, “nd” refers to “not determined.”

Dump B, from the sieve >150 μm, has an average grain size between 203 and 262 μm (see Figure 4b), with a distribution between 100 and 450 μm. Also, more than half (55%) of the observed grains are dark; yellow/brown grains are the next most abundant (30%), followed by red (9%) and white (8%) grains (Figure 4b). A subtle correlation is observed between grain size and color for piles A and B. In particular, dark grains in dump A are, on average, smaller than the other grains, with the opaque light grains being the largest. The color distribution of dump B seems to skew more toward dark grains compared to dump A. The image of dump B was taken at night and illuminated with white LEDs and histogram equalized to the

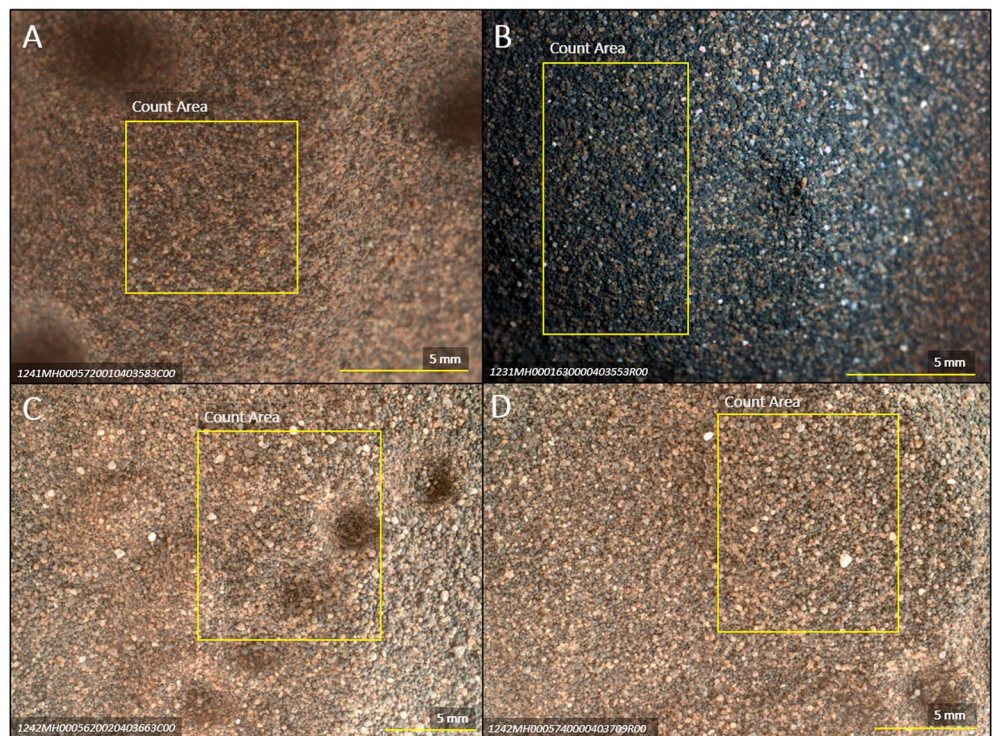


Figure 3. MAHLI images of the four dump piles: (A) dump A (<150 μm sieve size); (B) dump B (>150 μm sieve size); (C) dump C (150 μm–1 mm sieve size); (D) dump D (>1 mm sieve size). Count areas highlighted in yellow correspond to the areas used for the grain size estimation and color observations.

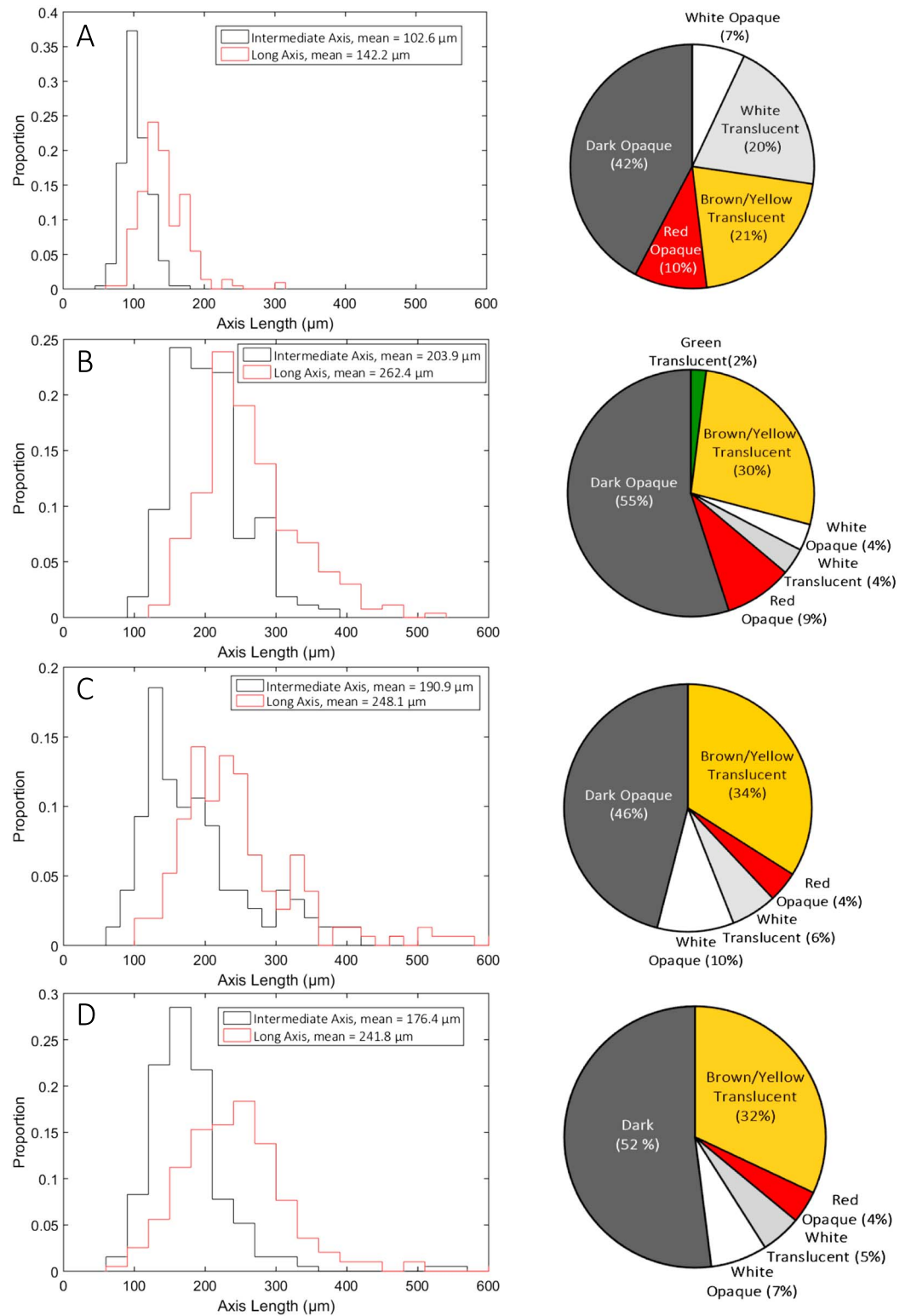


Figure 4. Analysis of grain size for the four dumps based on MAHLI images, with distributions of intermediate and long axes plotted on the left (from a grid-by-number approach) and the distribution of grain colors on the right. (A) Dump A; (B) dump B; (C) dump C; (D) dump D.

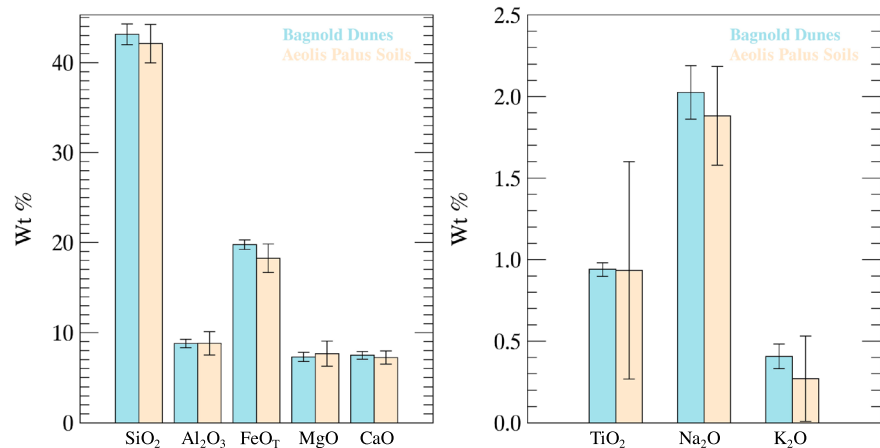


Figure 5. Histogram of average chemical composition for the Namib dune (blue) and Aeolis Palus soils (beige). For clarity, SiO₂, Al₂O₃, FeO, MgO, and CaO contents are displayed on the left plot and TiO₂, Na₂O, and K₂O contents on the right plot. The error bars correspond to the dispersion for each data set (standard deviation). These data are not normalized to 100% (i.e., the percentage of missing elements corresponds to the abundance of elements not yet systematically quantified by ChemCam).

other images to remove any skew in the color characterization of this image resulting from its lighting conditions.

Dump C (nominally 150 to 1000 μm) has an average size of 191 μm , with a distribution between 70 and 420 μm (Figure 4c). In this dump, like in the others, the dark grains are the most frequently observed (46%), but the yellow/brown grains are found in greater proportions than in the other dumps (34%; Figure 4c). Another particularity of this dump is that there is a clear correlation between the grain size and their color: the dark grains (~ 167 μm) are, on average, smaller than the yellow/brown grains (~ 179 μm) and the white/gray grains that are coarser (~ 243 μm).

Finally, dump D (from the >1 mm sieve) is similar to dump C. In fact, a discrete dump pile was not created at the expected dump D location, likely due to the fact that no grains >1 mm in size are present [Ehlmann *et al.*, 2017]. At the dump D location, the average grain size (likely derived from dump C sample) is ~ 176 μm (ranging from 70 to 350 μm ; Figure 4d). The significant difference between the sieve size and measured grain size may be due to clumped grains that did not pass through the >1 mm sieve. The dark grains are the majority (52%), 32% are yellow/brown, and 12% are gray and white grains (Figure 4d). The same kind of trend as dump C is observed between the size and the color, the dark grains being the smallest (~ 155 μm on average) and the gray/white ones being the largest, around 228 μm on average. Note that all of these grains, whatever their color, are <500 μm , and therefore, they all are smaller than the laser spot size.

In summary, Bagnold dunes and nearby soils contain grains that range from smaller than the laser spot size (<0.5 mm) and up to coarse sand, except dump A that corresponds to finer particles <150 μm only. This grain size investigation from the RMI and MAHLI images shows that the Bagnold dunes have few grains larger than 0.5 mm, and the MAHLI images also revealed that the dunes are depleted in <100 μm size fraction. The average size of the intermediate axis is 170–200 μm for dumps B, C, and D and only 100 μm for dump A, whereas the maximum axis measures on average 240–260 μm for the coarsest grains (dumps B, C, and D) and only 142 μm for dump A. The investigation of the MAHLI images for the dump piles has shown a distribution between 70 and 250 μm on average, which is similar to the results of Ehlmann *et al.* [2017]. Thus, ChemCam LIBS data are expected to sample multiple grains with each laser shot.

3.2. Chemistry

3.2.1. Comparison Between Average Composition of the Bagnold Dunes and Previous Soils

The major element composition of the Bagnold dunes, obtained by averaging all the data acquired by ChemCam in this area (including disturbed and undisturbed parts of the dunes, as well as dump piles), is similar to the average composition of the Aeolis Palus soils (Figure 5). Overall, the dispersion of the Bagnold dune data is lower for all oxides. TiO₂ contents, which tend to be quite variable in Aeolis Palus soils, are clearly

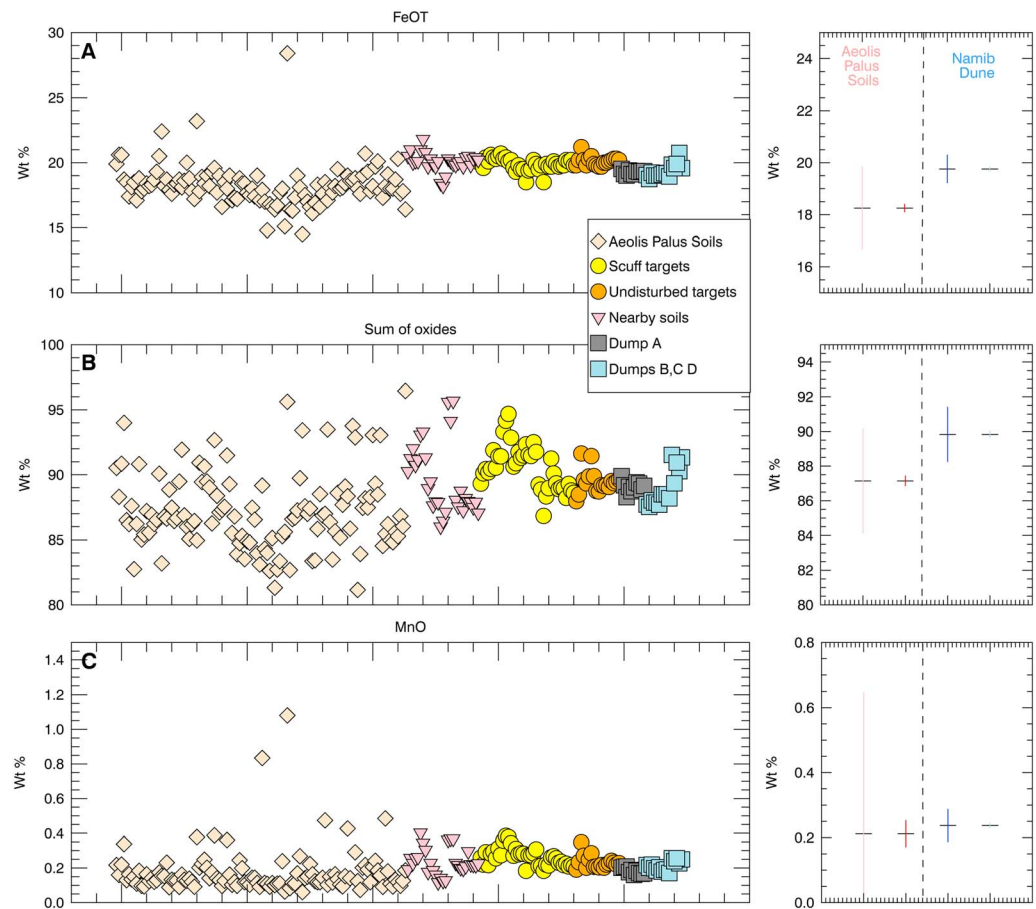


Figure 6. (A) FeO_T content; (B) sum of quantified oxides; (C) MnO content—along the traverse for Aeolis Palus soils, soils in the vicinity of the Bagnold dunes, and in the Bagnold dunes samples. Within each of these categories, targets are displayed by chronological order in order to highlight the variation when approaching the dunes. The right part of each plot shows the average for FeO_T (part A), sum of oxides (part B), and MnO (part C) for the Aeolis Palus soils and for the Bagnold dunes. The standard deviation is displayed in pink for the Aeolis Palus soils and in blue for Bagnold dunes; the uncertainty of the mean is displayed in brown for the Aeolis Palus soils and in light blue for Bagnold dunes. Average of FeO_T , sum of oxides, and MnO are higher in the dunes compared to the Aeolis Palus soils, with a smaller dispersion and a smaller uncertainty of the mean.

much less variable in the dunes compared to the Aeolis Palus soils, even though the mean values approximate each other. Na_2O and K_2O abundances measured in the dunes are in the upper half of the range observed for Aeolis Palus soils but still well within it. In fact, the only significant difference in bulk composition between the Bagnold dunes and the Aeolis Palus soils is the slight enrichment of the former in FeO_T . This difference can be better demonstrated by plotting all data points by category and chronological order (Figure 6a). On this figure, FeO_T content clearly increased (and dispersion decreased) after the Aeolis Palus soils as the rover approached the Bagnold dunes. This difference is significant, as observed in Figure 6a with the average FeO_T .

Another difference between the Bagnold dunes and the previously observed soils concerns the sum of oxides. The ChemCam quantification method [Clegg *et al.*, 2017] does not force the total of major-element abundances to be equal to 100 wt %, allowing the indirect measurement of a “missing” chemical component, which is the sum of oxides/elements that are not individually quantified. Mission experience has shown that a low sum of oxides is usually associated with targets enriched in volatile and moderately volatile elements such as H, S, Cl, and P (e.g., the purest Ca-sulfate veins sampled by ChemCam have sum of oxides as low as ~40 wt %, in agreement with the calcium oxide mass fraction of calcium sulfates) [Nachon *et al.*, 2017]. Figure 6b shows that the sum of oxides is less scattered and clearly higher in the Bagnold dunes than in the Aeolis Palus soils. This difference is statistically significant, as also demonstrated in Figure 7, as the

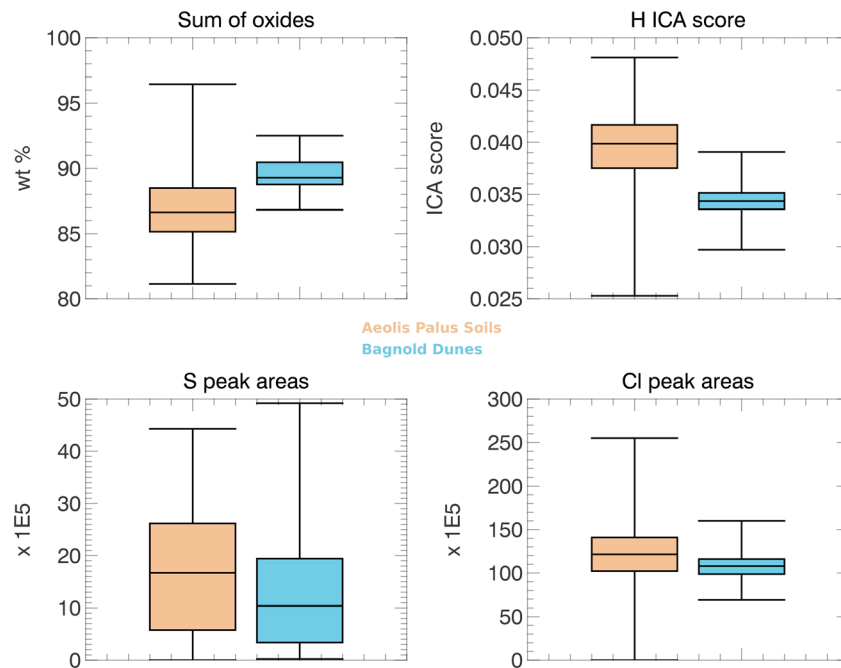


Figure 7. Boxplot distribution of the sum of major elements (expressed as oxides), of the H ICA score, and of Cl and S peak areas measured in the Aeolis Palus soils (beige) and in the Bagnold dunes (blue).

average sum of oxides of the Bagnold dune data is above the third quartile of the Aeolis Palus soils. As mentioned above, the higher sum of oxides suggests that the dunes contain less volatiles than the soils encountered along the traverse. This is confirmed in Figure 7, where we compare the S, Cl, and H signals from the spectra acquired in the dunes and in the Aeolis Palus soils. The S and Cl signals are presented in terms of peak area, as these elements are yet to be quantified by ChemCam [Wiens *et al.*, 2013]. Both elements show an average intensity lower in the Bagnold dunes, and the Cl signal is clearly less dispersed in the dunes. The H signal is significantly lower in the Bagnold dunes, with an average and third quartile lower than the first quartile obtained from the Aeolis Palus soils.

Finally, compared to Aeolis Palus soils, the Bagnold dunes and nearby soils present similar abundances in minor elements, except MnO. Indeed, MnO contents significantly increased when the rover arrived at the Bagnold dunes and remained higher and less scattered within the dune field (Figure 6c), although this difference is less significant than that of the sum of oxides and FeO_T content.

3.2.2. Intradune Observations

When looking at the data from the Bagnold dunes' targets only, some variations can be highlighted, even though they show an overall similar chemistry (Figures 5 and 6). Some of them such as Awasib and Doros show a correlation between their alkali and their silica and aluminum contents; all these elements being enriched compared to other targets (Figure 8). These samples are scuff targets from High and Namib dunes, respectively.

Mineralogical mixing trends can also be observed using the shot-to-shot data (where spectra corresponding to 30 individual laser shots within each observation point are investigated separately instead of being averaged), as the grains are overall smaller than the laser beam. Figure 9 shows the Na_2O versus MgO content and the Na_2O versus Al_2O_3 , for dump A (the finest grain size, $<150\ \mu\text{m}$ in Figure 9a); dump piles B, C, and D that are coarser-grained (average comprised between 170 and 260 μm in Figure 9b); and Barby_ccam3 and Doros targets in Figure 9c. Barby_ccam3 is part of the undisturbed crest of High dune and is one of the coarsest targets analyzed by ChemCam (see section 3.1), with only 53% of grains smaller than 0.5 mm. Doros is a disturbed soil from Namib dune and one of the finest-grained targets analyzed during the campaign (97% of the grains are $<0.5\ \text{mm}$). Data points from dump A plot in a relatively tight cluster, resulting in a low dispersion compared to the other dumps and suggesting an intimate mixture of fine-grained phases at the LIBS scale. In contrast, data points from dumps B, C, and D (in blue) show a mixing trend involving a Na_2O - and

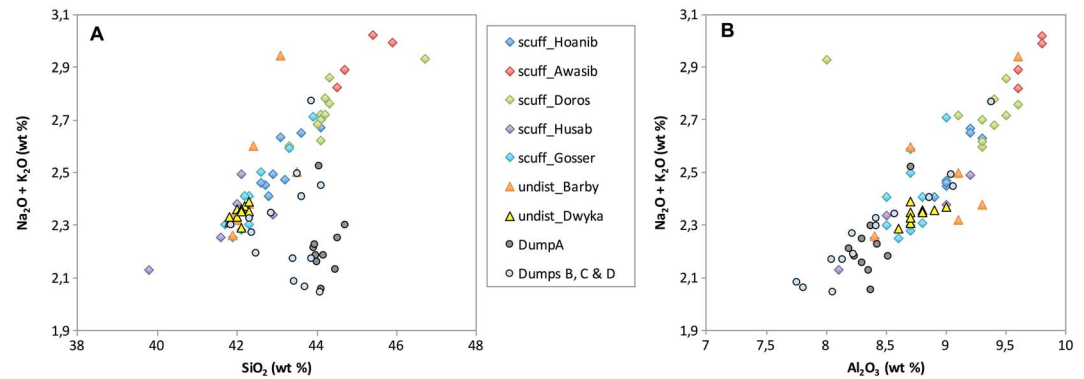


Figure 8. (A) $\text{Na}_2\text{O} + \text{K}_2\text{O}$ versus SiO_2 and (B) $\text{Na}_2\text{O} + \text{K}_2\text{O}$ versus Al_2O_3 for Bagnold dune targets. Awasib and Doros, two scuffed targets, are enriched in alkali and SiO_2 . Dump A and some points from dump B are clearly different from the other data, with less alkali.

Al_2O_3 -rich component. This suggests that, for coarser grain sizes approaching the scale of the laser beam such as dumps B, C, and D, ChemCam can observe the heterogeneity of a mixture of different mineralogical components, such as felsic and mafic. However, no pure end-member has been sampled, which implies that the grains, although closer to the size of the laser beam, are still smaller. Concerning Barby_ccam3 and Doros, we observe for both targets (in more extent for Barby_ccam3), as for dumps B, C, and D, a mixture between felsic and mafic components. A negative correlation is also observed between Na_2O and MgO , which is less obvious for dumps B, C, and D. Therefore, the chemical analysis also reveals indirectly that all dune samples containing grains larger than $150\ \mu\text{m}$ —i.e., all unsieved targets, as well as dump piles B, C, and D—are equivalent in term of grain sizes, despite slight differences in the coarsest size fractions (as revealed by the analysis of RMI images; Table 3). In contrast, dump A is really a different type of sample with a significantly lower grain size resulting in a more intimate mixture. Dump A is also depleted in FeO and MgO but enriched in Al_2O_3 and thus seems to be enriched in a feldspar-rich component (and conversely depleted in mafic phases) compared to the other dumps and dune materials. This seems consistent with the results from the MAHLI image analyses, where the white and brown/yellow grains (which could correspond to felsic phases) are more abundant than the darker grains in dump A compared to the other dumps (Figure 4). This observation seems also consistent with the mineralogy obtained from CheMin for the $<150\ \mu\text{m}$ size fraction (same material as dump A), where the most abundant phase corresponds to feldspars (37%), followed by olivine (26%) [Achilles *et al.*, 2017].

Minor elements also show some variations among the dune samples as a function of their grain sizes. Figure 7 has shown that the dunes contain overall less S, Cl, and H than the Aeolis Palus soils, despite a higher variability toward high values of S signal in the dunes. Indeed, dump A shows a slightly stronger S signal than all the other dune samples (Figure 10). This could partly explain the overall lower sum of oxides observed in dump A (Figure 6). Moreover, the dunes contain more MnO than Aeolis Palus soils, except dump A (Figure 6c). MnO is positively correlated with FeO and MgO , showing that the coarser grains (dumps B, C, and D) are more enriched in these mafic elements.

4. Discussion

The comparison of the Bagnold dunes with the Aeolis Palus soils has shown that they are overall similar in composition. Nevertheless, the Bagnold dunes present a lower dispersion in composition than the Aeolis Palus soils (Figures 5 and 6). Three hypotheses could explain this: (1) Aeolis Palus soils are sourced from a greater diversity of geological units, or conversely, that the Bagnold dune material originates from a more restricted geological area; (2) a mineralogical sorting that reduces the chemical variability within the dunes; or (3) a smaller grain size of the dunes compared to Aeolis Palus soils, small enough to measure only an average of several grains. The third hypothesis is more difficult to verify, as MAHLI images have not been acquired for each soil analysis along the traverse. However, Figure 4 shows that a majority of the grains correspond to dark grains, which tends to favor the second hypothesis, with a mineralogical sorting within the dunes

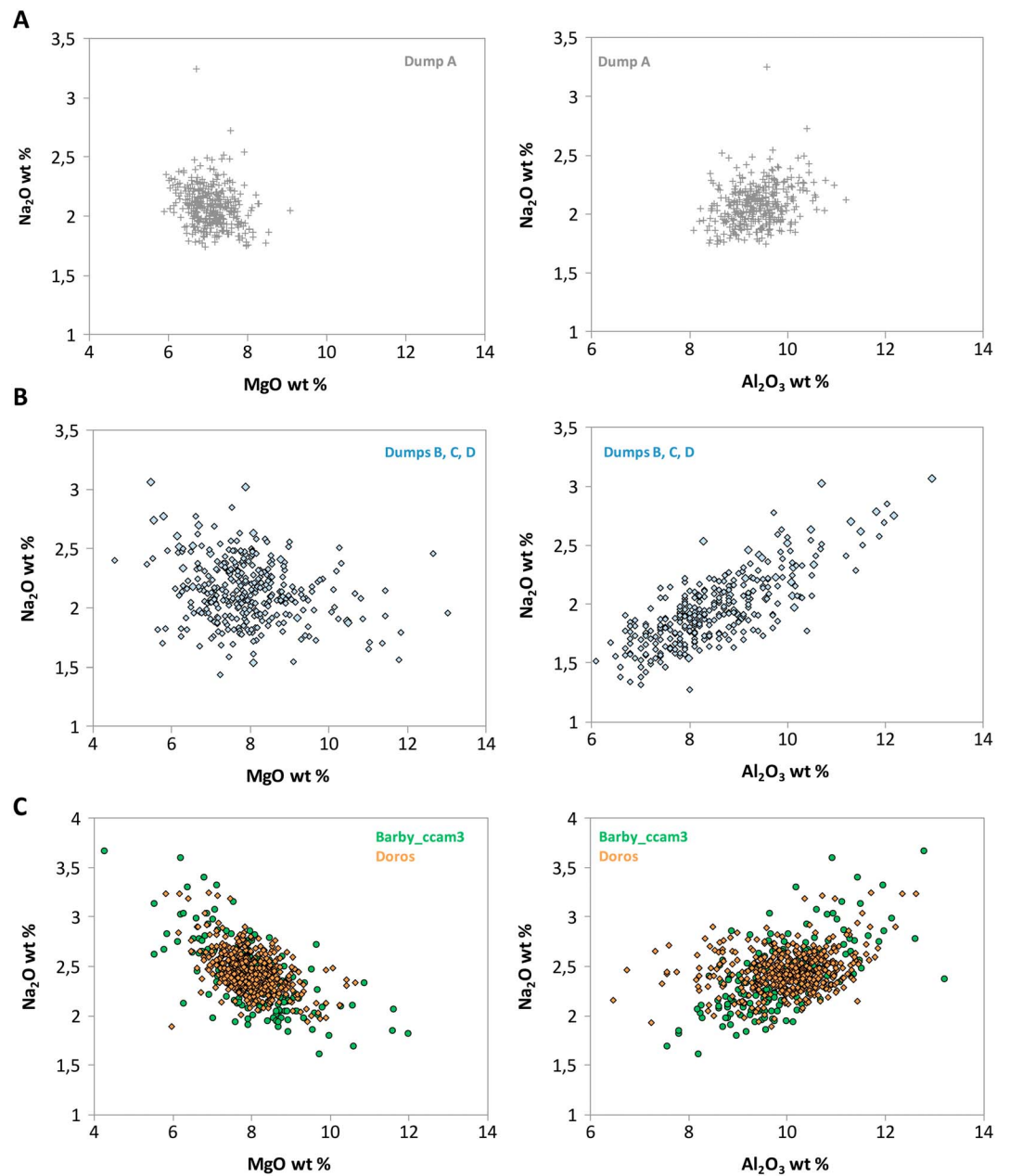


Figure 9. (left) Na_2O versus MgO and (right) Na_2O versus Al_2O_3 for several types of targets: (A) dump A, the finest grain size fraction ($<150\ \mu\text{m}$); (B) dumps B, C, and D made of coarser grains ($170\text{--}250\ \mu\text{m}$); (C) Barby_ccam3 and Doros, where Barby_ccam3 represents the coarsest dune sample (but still $<0.5\ \text{mm}$) and Doros represents one of the finest (but still $>150\ \mu\text{m}$).

compared to Aeolis Palus soils. This mineralogical sorting seems to have affected other aeolian deposits studied in Meridiani Planum [McGlynn *et al.*, 2012] and Gusev crater [McGlynn *et al.*, 2011; Sullivan *et al.*, 2008].

In addition to the compositional dispersion, the most striking difference is the larger sum of oxides in the dunes. As mentioned earlier, this reflects the lower abundance in the dunes of some elements not quantified by ChemCam, which include some volatile elements like H, S, P, and Cl. The lower H, S, and Cl signals observed in the Bagnold dunes are thus consistent with this interpretation. This is also consistent with the measurements made by the DAN instrument, which indicate a water content of $\sim 0.8\ \text{wt}\ \%$ in the dunes, which corresponds to at least 50% less than the average value of water abundance measured along the Curiosity traverse by this instrument (between 2 and 3%) [Ehlmann *et al.*, 2017]. SAM also found a low

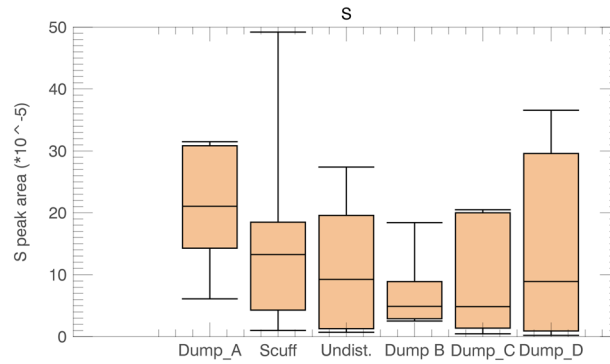


Figure 10. Boxplot distribution of the S signal measured in the dune material: all the dump piles as well as disturbed and undisturbed portions of the dunes.

water content in the dunes (~1 wt %), which is about half the content measured at Rocknest sand shadow [Sutter *et al.*, 2017]. The lower S and Cl LIBS signals are in agreement with the lower S and Cl abundances measured by the APXS [O’Connel-Cooper *et al.*, 2017] and the smaller release of sulfur dioxide measured by SAM [Sutter *et al.*, 2017].

The analysis of the Rocknest sand shadow early in the mission revealed the presence in the Aeolis Palus soils of an abundant amorphous component [Blake *et al.*, 2013; Bish *et al.*, 2013]. SAM and ChemCam analyses showed that this amorphous component was volatile-rich [Leshin *et al.*, 2013; Meslin *et al.*, 2013]. Results obtained in the Bagnold dunes could be interpreted in different ways. First, it is possible that an amorphous component of similar volatile content is present in lower abundance in the dune material. However, the proportion of amorphous component estimated from CheMin data at Gobabeb is the same, within uncertainties, as at Rocknest sand shadow, i.e., $35 \pm 15\%$ versus $27 \pm 14\%$ [Achilles *et al.*, 2017; Bish *et al.*, 2013]. But the Bagnold dunes may also contain more anhydrous volcanic or impact glass, which would account for a fraction of the amorphous component seen by CheMin. The second possible explanation (not incompatible with the previous one) is that the amorphous component present in the Bagnold dunes is less hydrated than Aeolis Palus soils (note that both the composition and hydration level of Aeolis Palus soils and fine-grained Rocknest targets are very similar) [Meslin *et al.*, 2013; Cousin *et al.*, 2014a]. In both cases, this interpretation suggests that the dune material has undergone less chemical alteration than Aeolis Palus soils. Another hypothesis would be that the $<100 \mu\text{m}$ size fraction, possibly including dust [Ehlmann *et al.*, 2017; Yen *et al.*, 2005], which is depleted in the dunes material (Figure 4), is the main carrier of this volatile-rich amorphous

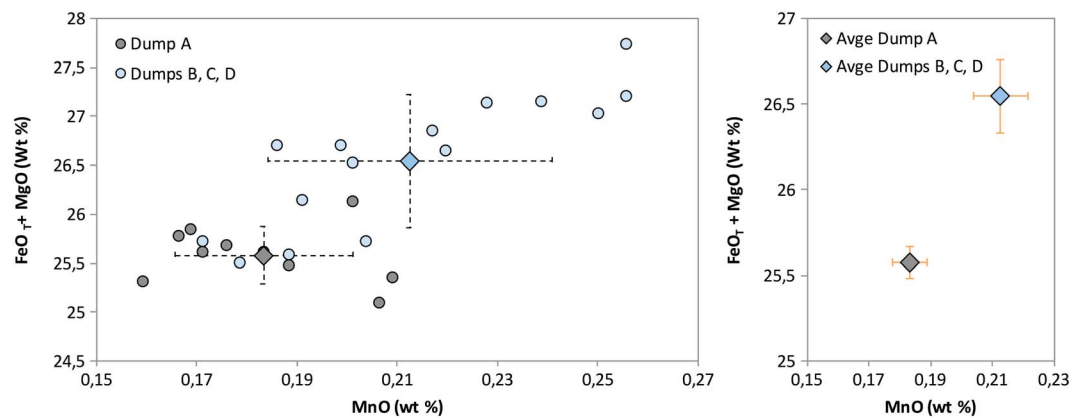


Figure 11. (left) MgO + FeO_T versus MnO content predicted in dump A and dumps B, C, and D at Namib dune. The diamond represents the average for each population (grey: dump A, blue: dumps B, C, and D), and the dashed error bars represent the standard deviation. (right) MgO + FeO_T versus MnO content in dump A and dumps B, C, and D, displaying only the average for each population (grey: dump A, blue: dumps B, C, and D), with orange error bars representing the uncertainty of the mean. This shows the difference of dump A from dumps B, C, and D more easily.

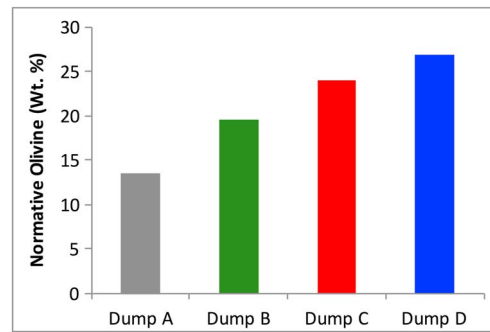


Figure 12. Normative olivine calculated in the different dumps, based on ChemCam analyses.

component and was removed by physical sorting during dune formation and transport. Also, the lower sulfur and chlorine signals could reflect lower abundances of sulfates, reduced sulfur phases, and perchlorates, which were identified by SAM in Rocknest samples [Leshin *et al.*, 2013], although at levels that were below CheMin's detection limit. Sulfur and chlorine could also be adsorbed onto soil grains, as a result of volcanic aerosol deposition or interaction with volcanic gases, in which case their lower abundance could be related to a smaller specific surface area of dune grains. Since the dunes are active, it is also possible that mechanical alteration of these grains has removed a volatile-rich coating, the conditions for its renewed formation not having been met since.

The enrichment in mafic minerals in the Bagnold dunes' material, evidenced by a small enrichment in olivine in the CheMin analysis (26 wt % of the crystalline phases [Achilles *et al.*, 2017] versus 22 wt % seen in Rocknest) is thus observed in the global ChemCam data set through the enrichment seen in FeO and MnO (Figures 6a and 6c). When restricting the analysis to the Bagnold dunes material, MgO is seen to correlate with FeO and MnO, confirming the presence of ferro-magnesian phases in the dunes such as olivine (Figure 11).

The enrichment seen in MgO, FeO, and MnO in the coarser grains (not analyzed by CheMin) suggests the presence of a greater proportion of mafic phases such as olivine in this material. This is consistent with the increase in olivine normative content calculated from the ChemCam data (Figure 12). This is also consistent with the previous conclusion about the lower abundance of volatile-rich amorphous component in the coarse grain size fraction. This suggests that the small olivine enrichment seen in the CheMin analysis (+4 wt % in the crystalline phases compared to Rocknest) actually provides a lower limit to the olivine content of these grains. MAHLI images have also revealed that dump A contains less dark grains (possibly olivine grains; see section 3.1) than the other, coarser-grained dumps. Moreover, these dark grains are the most abundant in the dunes, even if they have an average size somewhat smaller than grains of other colors. This could partly explain the strong olivine enrichment of High and Namib dunes (and other barchans within the Bagnold dune field) seen from orbital spectroscopy (olivine content ~15–22 wt %) [Rogers and Bandfield, 2009; Lane and Christensen, 2013; Seelos *et al.*, 2014; Lapotre *et al.*, 2017]. Such an enrichment in olivine is in agreement with the hypothesis that the material forming the dune (at least its coarser fraction) has experienced less chemical alteration than Aeolis Palus soils or that the most altered size fraction was partly removed by physical sorting. It is noteworthy that Sullivan *et al.* [2008] have suggested that olivine may be more resistant to mechanical weathering compared to other minerals under Mars climate, which could explain the enrichment in olivine in such active dunes. Although olivine is clearly observed in the dunes, feldspar phases are also detected: either as coarser grains when looking at the shot-to-shot analyses or due to their higher proportion in the finer-grained soils.

Soils located north of the Bagnold dune field are similar to the dunes in terms of grain sizes and compositions (Table 3 and Figure 6), which is consistent with the passive observations as well [Johnson *et al.*, 2017]. This seems to show that these dark soils are isolated patches of sediments that (1) could have been left behind by the migrating dunes or (2) are being incorporated in the dunes. Thus, the similarity of the nearby soils provides clues about the provenance and/or transport of the dune material.

5. Conclusions

The Bagnold Dunes Campaign represents the first in situ characterization of an active dune field on another planet. *Curiosity* carried out an extensive investigation at two locations: a sand patch near High dune and Namib dune. The ChemCam instrument analyzed 12 samples in total of various target types, including

undisturbed surfaces of the dune (ripple crests or troughs), disturbed materials (wheel scuffs), and piles of sieved sands produced by the rover sampling system. With its small footprint ($<500\ \mu\text{m}$), ChemCam is well suited to analyze fine-grained soils and mineralogical mixing trends can be recognized in coarser size fractions. The data acquired from the Bagnold dunes are compared to the Aeolis Palus soils analyzed by ChemCam along the traverse, which correspond to a data set of 116 observation points.

Based on MAHLI images, the Bagnold dune field has been shown to be composed of fine grains, mainly around $170\text{--}220\ \mu\text{m}$, which implies that the ChemCam laser beam always sampled a mixture of grains, as revealed by the chemical trends between mafic and felsic phases seen in the ChemCam data set. The analysis of the MAHLI images from the sieved samples (dump piles) has revealed the lack of grains $>1\ \text{mm}$ and $<100\ \mu\text{m}$ size fractions.

The overall composition of the Bagnold dunes is similar to that of Aeolis Palus soils. Nevertheless, a few differences have been observed and detailed in this study. The material from the Bagnold dunes, mainly the coarser grains (i.e., all except dump A), is lower in volatile elements compared to the Aeolis Palus soils, suggesting that (1) they have experienced less chemical alteration than the soils analyzed along the traverse, or (2) they have lost their alteration rind during their transport, or (3) they have interacted less with volcanic gases or aerosols because of their possibly larger specific surface area, or (4) physical sorting, which led to a depletion of small-sized grains ($<100\ \mu\text{m}$) in the dune material, also reduced the proportion of the most altered size fraction. These observations suggest that the Bagnold dunes contain less volatile-rich amorphous component than the Aeolis Palus soils. The CheMin instrument finds the same proportion of amorphous component in the Bagnold dunes as at Rocknest sand shadow. However, CheMin sampled only the $<150\ \mu\text{m}$ size fraction, corresponding to the dump A target, which was shown to be enriched in S compared to other dune material. Moreover, the amorphous component detected by CheMin could also contain some anhydrous volcanic or impact glass.

In the Bagnold dunes, no pure mineralogical end-members were sampled due to the small size of the grains. However, a correlation between FeO_T , MgO , and MnO was observed, revealing an enrichment in olivine in the coarsest dune material (i.e., $>150\ \mu\text{m}$). The same correlation between grain size and mineralogy was observed at Gusev in the El Dorado ripple field, probably due to stronger mechanical behavior of olivine [Sullivan *et al.*, 2008]. This would imply that the small olivine enrichment observed by CheMin in the smallest size fraction ($<150\ \mu\text{m}$) in fact corresponds to a lower limit of the olivine enrichment in the dunes. Moreover, the analysis of the MAHLI images is consistent with a higher proportion of dark grains interpreted as olivine, rather than the presence of olivine grains of larger size.

The soils located north of the Bagnold dunes sampled a few sols before entering the dune field are similar to the dunes in both grain size and composition. This observation suggests that they correspond to patchy soils left behind during migration of the Bagnold dunes or that they represent a source region for the material incorporated in the dunes.

Acknowledgments

We are grateful to the MSL science and operation teams who developed the rover and contributed to collecting the Bagnold dune data set. All the data sets used in this paper are released and can be found on the Planetary Data Science (<http://pdsgeosciences.wustl.edu/missions/msl/.htm>). We also thank S. Karunatillake and S. Ruff for their helpful and constructive comments, which improved the manuscript. We would also like to express our sincere gratefulness to Nathan Bridges for his enthusiasm and huge implication for the Bagnold Dunes Campaign. This work was supported by the CNES in France and by the NASA Mars Exploration Program in the U.S.

References

- Anderson, R., and J. Bell III (2010), Geologic mapping and characterization of Gale Crater and implications for its potential as a Mars Science Laboratory site, *Mars*, 5, 76–128, doi:10.1555/mars.2010.0004.
- Anderson, D., et al. (2017), Characterization of laser-induced breakdown spectroscopy (LIBS) emission lines for the identification of chlorides, carbonates, and sulfates in salt/basalt mixtures for the application to MSL ChemCam data, *J. Geophys. Res. Planets*, 122, 744–770, doi:10.1002/2016JE005164.
- Anderson, R. B., S. M. Clegg, J. Frydenvang, R. C. Wiens, S. McLennan, R. V. Morris, B. Ehlmann, and M. D. Dyar (2017), Improved accuracy in quantitative laser-induced breakdown spectroscopy using sub-models, *Spectrochim. Acta, Part B*, 129, 49–57, doi:10.1016/j.sab.2016.12.002.
- Anderson, R. C., et al. (2012), Collecting Samples in Gale Crater Mars; an Overview of the Mars Science Laboratory Sample Acquisition Sample, *Space Sci. Rev.*, 170, 57–75.
- Achilles, C. N., et al. (2017), Mineralogy of an active aeolian sediment from the Namib dune, Gale Crater, Mars, *J. Geophys. Res. Planets*, 122, doi:10.1002/2017JE005262.
- Arvidson, R. E., and M. Maimone (2016), Curiosity rover mobility issues crossing Martian megaripple fields, *Proc. Lunar Planet. Sci. Conf.* 47th, 1137 pp.
- Bell, J. F., M. C. Malin, M. A. Caplinger, M. A. Ravine, A. S. Godber, M. C. Jungers, M. S. Rice, and R. B. Anderson (2012), Mastcam multispectral imaging on the Mars Science Laboratory rover: Wavelength coverage and imaging strategies at the Gale Crater field site, *Proc. Lunar Planet. Sci. Conf.* 43rd, 2541 pp.
- Bish, D., et al. (2013), X-Ray diffraction results from Mars Science Laboratory: Mineralogy of Rocknest at Gale Crater, *Science*, 341, doi:10.1126/science.1238932.
- Blake, D. F., et al. (2012), Characterization and calibration of the CheMin Mineralogical Instrument on Mars Science Laboratory, *Space Sci. Rev.*, 170, 341–399.

- Blake, D. F., et al. (2013), Curiosity at Gale Crater, Mars: Characterization and analysis of the Rocknest sand shadow, *Science*, *341*(6153), 1239505.
- Blaney, D., et al. (2014), Chemistry and texture of the rocks at "Rocknest," Gale Crater: Evidence for iron-rich cements, *J. Geophys. Res. Planets*, *119*, 2109–2131, doi:10.1002/2013JE004590.
- Bridges, N., R. Sullivan, C. E. Newman, S. Navarro, J. van Beek, R. C. Ewing, F. Ayoub, S. Silvestro, S. Le Mouélic, and W. Rapin (2017), Martian aeolian activity at the Bagnold dunes, Gale Crater: The view from the surface and orbit, *J. Geophys. Res. Planets*, *122*, doi:10.1002/2017JE005263.
- Bridges, N. T., and B. L. Ehlmann (2017), The Mars Science Laboratory (MSL) Bagnold Dunes campaign, Phase I: Overview and introduction to the special issue, *J. Geophys. Res. Planets*, *122*, doi:10.1002/2017JE005401.
- Campbell, J. L., G. M. Perrett, R. Gellert, S. M. Andruskenko, N. I. Boyd, J. A. Maxwell, P. L. King, and C. D. M. Schofield (2012), Calibration of the Mars Science Laboratory alpha particle X-ray spectrometer, *Space Sci. Rev.*, *170*, 319–340.
- Chojnacki, M., J. R. Johnson, J. E. Moersch, L. K. Fenton, T. I. Michaels, and J. F. Bell III (2015), Persistent aeolian activity at Endeavour crater Meridiani Planum Mars; new observations from orbit and the surface, *Icarus*, *251*, 275–290, doi:10.1016/j.icarus.2014.04.044.
- Clegg, S. M., E. Sklute, M. D. Dyar, J. E. Barefield, and R. C. Wiens (2009), Multivariate analysis of remote laser-induced breakdown spectroscopy spectra using partial least squares, principal component analysis, and related techniques, *Spectrochim. Acta, Part B*, *64*(1), 79–88.
- Clegg, S., et al. (2017), Recalibration of the Mars Science Laboratory ChemCam Instrument with an expanded geochemical database, *Spectrochim. Acta, Part B*, *129*, 64–85, doi:10.1016/j.sab.2016.12.003.
- Cousin, A., et al. (2014a), ChemCam blind targets: A helpful way of analyzing soils and rocks along the traverse, *Proc. Lunar Planet. Sci. Conf. 45th*, 1278 pp.
- Cousin, A., et al. (2014b), Compositions of coarse and fine particles in Martian soils at Gale: A window into the production of soils, *Icarus*, *249*, 22–42.
- Edgett, K. S., and Yingst R. A. (2013), Curiosity's Mars Hand Lens Imager (MAHLI): Sol 0–179 activities, observations, range and scale characterization, in *European Planetary Science Congress*, vol. 8, pp. EPSC2013-246, London.
- Ehlmann, B. L., et al. (2017), Chemistry, mineralogy, and grain properties at Namib and High dunes, Bagnold dune field, Gale crater, Mars: A synthesis of Curiosity rover observations, *J. Geophys. Res. Planets*, *122*, doi:10.1002/2017JE005267.
- Fabre, C., S. Maurice, A. Cousin, R. C. Wiens, O. Forni, V. Sautter, and D. Guillaume (2011), Onboard calibration igneous targets for the Mars Science Laboratory Curiosity rover and the Chemistry Camera laser induced breakdown spectroscopy instrument, *Spectrochim. Acta, Part B*, *66*, 280–289, doi:10.1016/j.sab.2011.03.01.
- Forni, O., S. Clegg, R. C. Wiens, S. Maurice, and O. Gasnault (2009), Multivariate analysis of ChemCam first calibration samples, *Proc. Lunar Planet. Sci. Conf. 40th*, 1523 pp.
- Forni, O., S. Maurice, O. Gasnault, R. C. Wiens, A. Cousin, S. M. Clegg, J.-B. Sirven, and J. Lasue (2013), Independent component analysis classification of laser induced breakdown spectroscopy spectra, *Spectrochim. Acta, Part B*, *86*, 31–41.
- Friday, M. E., C. M. Fedo, I. O. McGlynn, and H. Y. McSween (2013), The accuracy of 2D assessment of sediment textures, and application to Mars, *Proc. Lunar Planet. Sci. Conf. 44th*, 2361 pp.
- Graham, D. J., S. P. Rice, and I. Reid (2005), Comment: Photographic techniques for characterizing streambed particle sizes, *Trans. Am. Fish. Soc.*, *134*(6), 1599–1603.
- Grotzinger, J. P., et al. (2014), A habitable fluvio-lacustrine environment at Yellowknife Bay, Gale Crater, Mars, *Science*, *343*(6169), 1242777, doi:10.1126/science.1242777.
- Grotzinger, J. P., et al. (2015), Deposition, exhumation, and paleoclimate of an ancient lake deposit, Gale Crater, Mars, *Science*, *350*(6257), aac7575.
- Hyvarinen, A. (2001), Blind source separation by nonstationarity of variance: A cumulant-based approach, *IEEE Trans. Neural Networks*, *12*(6), 1471–1474.
- Johnson, J. R., et al. (2017), Visible/near-infrared spectral diversity from in situ observations of the Bagnold dune field sands in Gale Crater, Mars, *J. Geophys. Res. Planets*, *122*, doi:10.1002/2016JE005187.
- Karunatillake, S., S. M. McLennan, K. E. Herkenhoff, J. M. Husch, C. Hardgrove, and J. R. Skok (2014a), A Martian case study of segmenting images automatically for granulometry and sedimentology. Part 1: Algorithm, *Icarus*, *229*, 400–407, doi:10.1016/j.icarus.2013.10.001.
- Karunatillake, S., McLennan S. M., Herkenhoff K. E., Husch J. M., Hardgrove C., and Skok J.R. (2014b), A Martian case study of segmenting images automatically for granulometry and sedimentology. Part 2: Assessment, *Icarus*, *229*, 408–417, doi:10.1016/j.icarus.2013.09.021. [Available at <http://www.sciencedirect.com/science/article/pii/S0019103513004120>.]
- Lane, M. D., and P. R. Christensen (2013), Determining olivine composition of basaltic dunes in Gale Crater, Mars, from orbit: Awaiting ground truth from Curiosity, *Geophys. Res. Lett.*, *40*, 3517–3521, doi:10.1002/grl.50621.
- Langevin, Y., B. Gondet, S. Le Mouélic, O. Gasnault, K. Herkenhoff, D. Blaney, S. Maurice, R. Wiens, and the MSL Science Team (2013), Processing approaches for optimal science exploitation of the ChemCam Remote Microscopic Imager (RMI) during the first 90 days of curiosity operations, *Proc. Lunar Planet. Sci. Conf. 44th*, 1227 pp.
- Lanza, N. L., et al. (2014), High manganese concentrations in rocks at Gale Crater, Mars, *Geophys. Res. Lett.*, *41*, 5755–5763, doi:10.1002/2014GL060329.
- Lapotre, M., B. Ehlmann, S. E. Minson, R. E. Arvidson, F. Ayoub, A. Fraeman, R. C. Ewing, and N. T. Bridges (2017), Compositional variations in sands of the Bagnold dunes at Gale Crater, Mars, from visible-shortwave infrared spectroscopy and comparison with ground-truth from the Curiosity rover, *J. Geophys. Res. Planets*, *122*, doi:10.1002/2016JE005133.
- Lasue, J., R. C. Wiens, T. F. Stepinski, O. Forni, S. M. Clegg, and S. Maurice (2011), Nonlinear mapping technique for data visualization and clustering assessment of LIBS data: Application to ChemCam data, *Anal. Bioanal. Chem.*, *400*(10), 3247–3260.
- Le Mouélic, S., et al. (2015), The ChemCam Remote Micro-Imager at Gale Crater: Review of the first year on Mars, *Icarus*, *249*, 93–107.
- Leshin, L. A., et al. (2013), Volatile, isotope and organic analysis of Martian fines with the Mars Curiosity rover, *Science*, *341*, doi:10.1126/science.1238937.
- Malin, M. C., et al. (2010), The Mars Science Laboratory (MSL) mast-mounted cameras (Mastcams) flight instruments, *Proc. Lunar Planet. Sci. Conf. 41th*, 1123 pp.
- Mahaffy, P., S. K. Atreya, P. Conrad, C. Szopa, C. Webster, M. Cabane, and P. Coll (2012), The Sample Analysis at Mars (SAM) experiment onboard the MSL 2011 rover: Study of the present and past Mars surface environment through in situ chemical analyses, in *39th COSPAR Scientific Assembly*, vol. 39, 1143 pp.
- Mangold, N., et al. (2015), Chemical variations in Yellowknife Bay formation sedimentary rocks analyzed by ChemCam on board the Curiosity rover on Mars, *J. Geophys. Res. Planets*, *120*, 452–482, doi:10.1002/2014JE004681.

- Maurice, S., et al. (2012), The ChemCam instrument suite on the Mars Science Laboratory (MSL) rover: Science objectives and mast unit description, *Space Sci. Rev.*, *170*, 95–166, doi:10.1007/s11214-012-9912-2.
- Maurice, S., A. Cousin, R. Wiens, O. Gasnault, L. Parès, O. Forni, P. Y. Meslin, S. Clegg, and ChemCam Team (2013), Laser induced breakdown spectroscopy (LIBS) spot size at stand-off distances with ChemCam, *Proc. Lunar Planet. Sci. Conf.* *43th*, 1659 pp.
- Meslin, P. Y., et al. (2013), Soil diversity and hydration as observed by ChemCam at Gale Crater, Mars, *Science*, *341*(6153), 1238670.
- McGlynn, I. O., C. M. Fedo, and H. Y. McSween Jr. (2011), Origin of basaltic soils at Gusev crater, Mars, by aeolian modification of impact-generated sediment, *J. Geophys. Res.*, *116*, E00F22, doi:10.1029/2010JE003712.
- McGlynn, I. O., C. M. Fedo, and H. Y. McSween Jr. (2012), Soil mineralogy at the Mars Exploration Rover landing sites: An assessment of the competing roles of physical sorting and chemical weathering, *J. Geophys. Res.*, *117*, E01006, doi:10.1029/2011JE003861.
- McLennan, S. M., et al. (2014), Elemental geochemistry of sedimentary rocks at Yellowknife Bay, Gale Crater, Mars, *Science*, *343*(6169), 1244734.
- McSween, H. C. (1994), What we have learned about Mars from SNC meteorites, *Meteoritics*, *29*, 757–779.
- Milliken, R. E., J. P. Grotzinger, and B. J. Thomson (2010), Paleoclimate of Mars as captured by the stratigraphic record in Gale Crater, *Geophys. Res. Lett.*, *37*, L04201, doi:10.1029/2009GL041870.
- Mitrofanov, L. G., et al. (2012), Dynamic Albedo of Neutrons (DAN) experiment onboard NASA's Mars Science Laboratory, *Space Sci. Rev.*, *170*, 559–582, doi:10.1007/s11214-012-9924-y.
- Nachon, M., et al. (2017), Chemistry of diagenetic features analyzed by ChemCam at Pahrump Hills, Gale Crater, Mars, *Icarus*, *281*, 121–136, doi:10.1016/j.icarus.2016.08.026.
- O'Connell-Cooper, C. D., J. G. Spray, L. M. Thompson, R. Gellert, J. A. Berger, N. I. Boyd, E. D. Desouza, G. M. Perrett, M. Schmidt, and S. J. VanBommel (2017), APXS-derived chemistry of the Bagnold dune sands: Comparisons with Gale Crater soils and the global Martian average, *J. Geophys. Res. Planets*, *122*, doi:10.1002/2017JE005268.
- Rapin, W., et al. (2017), Quantification of water content by laser induced breakdown spectroscopy on Mars, *Spectrochim. Acta, Part B*, *130*, 82–100, doi:10.1016/j.sab.2017.02.007.
- Rogers, A. D., and J. L. Bandfield (2009), Mineralogical characterization of Mars Science Laboratory candidate landing sites from THEMIS and TES data, *Icarus*, *203*(2), 437–453, doi:10.1016/j.icarus.2009.04.020.
- Seelos, K. D., F. P. Seelos, C. E. Viviano-Beck, S. L. Murchie, R. E. Arvidson, B. L. Ehlmann, and A. A. Fraeman (2014), Mineralogy of the MSL Curiosity landing site in Gale Crater as observed by MRO/CRISM, *Geophys. Res. Lett.*, *41*, 4880–4887, doi:10.1002/2014GL060310.
- Schneider, C. A., W. S. Rasband, and K. W. Eliceiri (2012), NIH image to ImageJ: 25 years of image analysis, *Nat. Methods*, *9*, 671–675.
- Sullivan, R., et al. (2008), Wind-driven particle mobility on Mars: Insights from Mars Exploration Rover observations at “El Dorado” and surroundings at Gusev Crater, *J. Geophys. Res.*, *113*, E06S07, doi:10.1029/2008JE003101.
- Sutter, B., et al. (2017), Evolved gas analyses of sedimentary rocks and eolian sediment in Gale Crater, Mars: Results of the Curiosity rover's Sample Analysis at Mars (SAM) instrument from Yellowknife Bay to the Namib dune, *J. Geophys. Res. Planets*, *122*, doi:10.1002/2016JE005225.
- Wentworth, C. K. (1922), A scale of grade and class terms for clastic sediments, *J. Geol.*, *30*, 377–392.
- Wiens, R., et al. (2012), The ChemCam instrument suite on the Mars Science Laboratory (MSL) rover: Body unit and combined system performance, *Space Sci. Rev.*, *170*, 167–227.
- Wiens, R. C., et al. (2013), Pre-flight calibration and initial data processing for the ChemCam laser-induced breakdown spectroscopy instrument on the Mars Science Laboratory rover, *Spectrochim. Acta, Part B*, *82*, 1–27.
- Wiens R., et al. (2015), Major-element compositional diversity observed by ChemCam along the MSL traverse: The first three years, Abstract P43B-2124 presented at 2015 Fall Meeting, AGU, San Francisco, Calif., 14–18 Dec.
- Yen, A. S., et al. (2005), An integrated view of the chemistry and mineralogy of Martian soils, *Nature*, *436*, 49–54, doi:10.1038/nature03637.
- Yingst, R. A., L. Crumpler, W. H. Farrand, R. Li, N. A. Cabrol, and L. D. Neakrase (2008), Morphology and texture of particles along the Spirit rover traverse from sol 450 to sol 745, *J. Geophys. Res.*, *113*, E12S41, doi:10.1029/2008JE003179.
- Yingst, R. A., et al. (2013), Characteristics of pebble- and cobble-sized clasts along the Curiosity rover traverse from Bradbury Landing to Rocknest, *J. Geophys. Res. Planets*, *118*, 2361–2380, doi:10.1002/2013JE004435.
- Yingst, R. A., et al. (2016), Characteristics of pebble and cobble-sized clasts along the Curiosity rover traverse from sol 100 to 750: Terrain types, potential sources, and transport mechanisms, *Icarus*, *280*, 72–92, doi:10.1016/j.icarus.2016.03.001.